

Multi-Electron Production at High Transverse Momenta in ep Collisions at HERA

H1 Collaboration

Abstract

Multi-electron production is studied at high electron transverse momentum in positron- and electron-proton collisions using the H1 detector at HERA. The data correspond to an integrated luminosity of 115 pb^{-1} . Di-electron and tri-electron event yields are measured. Cross sections are derived in a restricted phase space region dominated by photon-photon collisions. In general good agreement is found with the Standard Model predictions. However, for electron pair invariant masses above 100 GeV, three di-electron events and three tri-electron events are observed, compared to Standard Model expectations of 0.30 ± 0.04 and 0.23 ± 0.04 , respectively.

A. Aktas¹⁰, V. Andreev²⁴, T. Anthonis⁴, A. Asmone³¹, A. Babaev²³, S. Backovic³⁵, J. Bähr³⁵, P. Baranov²⁴, E. Barrelet²⁸, W. Bartel¹⁰, S. Baumgartner³⁶, J. Becker³⁷, M. Beckingham²¹, O. Behnke¹³, O. Behrendt⁷, A. Belousov²⁴, Ch. Berger¹, T. Berndt¹⁴, J.C. Bizot²⁶, J. Böhme¹⁰, M.-O. Boenig⁷, V. Boudry²⁷, J. Bracinik²⁵, W. Braunschweig¹, V. Brisson²⁶, H.-B. Bröker², D.P. Brown¹⁰, D. Bruncko¹⁶, F.W. Büsser¹¹, A. Bunyatyan^{12,34}, G. Buschhorn²⁵, L. Bystritskaya²³, A.J. Campbell¹⁰, S. Caron¹, F. Cassol-Brunner²², V. Chekelian²⁵, D. Clarke⁵, C. Collard⁴, J.G. Contreras^{7,41}, Y.R. Coppens³, J.A. Coughlan⁵, M.-C. Cousinou²², B.E. Cox²¹, G. Cozzika⁹, J. Cvach²⁹, J.B. Dainton¹⁸, W.D. Dau¹⁵, K. Daum^{33,39}, B. Delcourt²⁶, N. Delerue²², R. Demirchyan³⁴, A. De Roeck^{10,43}, E.A. De Wolf⁴, C. Diaconu²², J. Dingfelder¹³, V. Dodonov¹², J.D. Dowell³, A. Dubak²⁵, C. Duprel², G. Eckerlin¹⁰, V. Efremenko²³, S. Egli³², R. Eichler³², F. Eisele¹³, M. Ellerbrock¹³, E. Elsen¹⁰, M. Erdmann^{10,40,e}, W. Erdmann³⁶, P.J.W. Faulkner³, L. Favart⁴, A. Fedotov²³, R. Felst¹⁰, J. Ferencei¹⁰, M. Fleischer¹⁰, P. Fleischmann¹⁰, Y.H. Fleming³, G. Flucke¹⁰, G. Flügge², A. Fomenko²⁴, I. Foresti³⁷, J. Formánek³⁰, G. Franke¹⁰, G. Frising¹, E. Gabathuler¹⁸, K. Gabathuler³², J. Garvey³, J. Gassner³², J. Gayler¹⁰, R. Gerhards¹⁰, C. Gerlich¹³, S. Ghazaryan³⁴, L. Goerlich⁶, N. Gogitidze²⁴, S. Gorbounov³⁵, C. Grab³⁶, V. Grabski³⁴, H. Grässler², T. Greenshaw¹⁸, M. Gregori¹⁹, G. Grindhammer²⁵, D. Haidt¹⁰, L. Hajduk⁶, J. Haller¹³, G. Heinzlmann¹¹, R.C.W. Henderson¹⁷, H. Henschel³⁵, O. Henshaw³, R. Heremans⁴, G. Herrera^{7,44}, I. Herynek²⁹, M. Hildebrandt³⁷, K.H. Hiller³⁵, J. Hladký²⁹, P. Höting², D. Hoffmann²², R. Horisberger³², A. Hovhannisyan³⁴, M. Ibbotson²¹, M. Jacquet²⁶, L. Janauschek²⁵, X. Janssen⁴, V. Jemanov¹¹, L. Jönsson²⁰, C. Johnson³, D.P. Johnson⁴, H. Jung^{20,10}, D. Kant¹⁹, M. Kapichine⁸, M. Karlsson²⁰, J. Katzy¹⁰, F. Keil¹⁴, N. Keller³⁷, J. Kennedy¹⁸, I.R. Kenyon³, C. Kiesling²⁵, M. Klein³⁵, C. Kleinwort¹⁰, T. Kluge¹, G. Knies¹⁰, B. Koblitz²⁵, S.D. Kolya²¹, V. Korbel¹⁰, P. Kostka³⁵, R. Koutouev¹², A. Kropivnitskaya²³, J. Kroseberg³⁷, J. Kueckens¹⁰, T. Kuhr¹⁰, M.P.J. Landon¹⁹, W. Lange³⁵, T. Laštovička^{35,30}, P. Laycock¹⁸, A. Lebedev²⁴, B. Leißner¹, R. Lemrani¹⁰, V. Lendermann¹⁰, S. Levonian¹⁰, B. List³⁶, E. Lobodzinska^{10,6}, N. Loktionova²⁴, R. Lopez-Fernandez¹⁰, V. Lubimov²³, H. Lueders¹¹, S. Lüders³⁷, D. Lücke^{7,10}, L. Lytkin¹², A. Makankine⁸, N. Malden²¹, E. Malinovski²⁴, S. Mangano³⁶, P. Marage⁴, J. Marks¹³, R. Marshall²¹, H.-U. Martyn¹, J. Martyniak⁶, S.J. Maxfield¹⁸, D. Meer³⁶, A. Mehta¹⁸, K. Meier¹⁴, A.B. Meyer¹¹, H. Meyer³³, J. Meyer¹⁰, S. Michine²⁴, S. Mikocki⁶, D. Milstead¹⁸, F. Moreau²⁷, A. Morozov⁸, J.V. Morris⁵, K. Müller³⁷, P. Murín^{16,42}, V. Nagovizin²³, B. Naroska¹¹, J. Naumann⁷, Th. Naumann³⁵, P.R. Newman³, F. Niebergall¹¹, C. Niebuhr¹⁰, D. Nikitin⁸, G. Nowak⁶, M. Nozicka³⁰, B. Olivier¹⁰, J.E. Olsson¹⁰, D. Ozerov²³, C. Pascaud²⁶, G.D. Patel¹⁸, M. Peez²², E. Perez⁹, A. Petrukhin³⁵, D. Pitzl¹⁰, R. Pöschl²⁶, B. Povh¹², N. Raicevic³⁵, J. Rauschenberger¹¹, P. Reimer²⁹, B. Reisert²⁵, C. Risler²⁵, E. Rizvi³, P. Robmann³⁷, R. Roosen⁴, A. Rostovtsev²³, S. Rusakov²⁴, K. Rybicki^{6,†}, D.P.C. Sankey⁵, E. Sauvan²², S. Schätzel¹³, J. Scheins¹⁰, F.-P. Schilling¹⁰, P. Schleper¹⁰, D. Schmidt³³, S. Schmidt²⁵, S. Schmitt³⁷, M. Schneider²², L. Schoeffel⁹, A. Schöning³⁶, V. Schröder¹⁰, H.-C. Schultz-Coulon⁷, C. Schwanenberger¹⁰, K. Sedlák²⁹, F. Sefkow¹⁰, I. Sheviakov²⁴, L.N. Shtarkov²⁴, Y. Sirois²⁷, T. Sloan¹⁷, P. Smirnov²⁴, Y. Soloviev²⁴, D. South²¹, V. Spaskov⁸, A. Specka²⁷, H. Spitzer¹¹, R. Stamen¹⁰, B. Stella³¹, J. Stiewe¹⁴, I. Strauch¹⁰, U. Straumann³⁷, G. Thompson¹⁹, P.D. Thompson³, F. Tomasz¹⁴, D. Traynor¹⁹, P. Truöl³⁷, G. Tsipolitis^{10,38}, I. Tsurin³⁵, J. Turnau⁶, J.E. Turney¹⁹, E. Tzamariudaki²⁵, A. Uraev²³, M. Urban³⁷, A. Usik²⁴, S. Valkár³⁰, A. Valkárová³⁰, C. Vallée²², P. Van Mechelen⁴, A. Vargas Trevino⁷, S. Vassiliev⁸, Y. Vazdik²⁴, C. Veelken¹⁸, A. Vest¹, A. Vichnevski⁸, V. Volchinski³⁴, K. Wacker⁷, J. Wagner¹⁰,

B. Waugh²¹, G. Weber¹¹, R. Weber³⁶, D. Wegener⁷, C. Werner¹³, N. Werner³⁷, M. Wessels¹, B. Wessling¹¹, M. Winde³⁵, G.-G. Winter¹⁰, Ch. Wissing⁷, E.-E. Woehrling³, E. Wünsch¹⁰, J. Žáček³⁰, J. Zálešák³⁰, Z. Zhang²⁶, A. Zhokin²³, F. Zomer²⁶, and M. zur Nedden²⁵

¹ *I. Physikalisches Institut der RWTH, Aachen, Germany^a*

² *III. Physikalisches Institut der RWTH, Aachen, Germany^a*

³ *School of Physics and Space Research, University of Birmingham, Birmingham, UK^b*

⁴ *Inter-University Institute for High Energies ULB-VUB, Brussels; Universiteit Antwerpen (UIA), Antwerpen; Belgium^c*

⁵ *Rutherford Appleton Laboratory, Chilton, Didcot, UK^b*

⁶ *Institute for Nuclear Physics, Cracow, Poland^d*

⁷ *Institut für Physik, Universität Dortmund, Dortmund, Germany^a*

⁸ *Joint Institute for Nuclear Research, Dubna, Russia*

⁹ *CEA, DSM/DAPNIA, CE-Saclay, Gif-sur-Yvette, France*

¹⁰ *DESY, Hamburg, Germany*

¹¹ *Institut für Experimentalphysik, Universität Hamburg, Hamburg, Germany^a*

¹² *Max-Planck-Institut für Kernphysik, Heidelberg, Germany*

¹³ *Physikalisches Institut, Universität Heidelberg, Heidelberg, Germany^a*

¹⁴ *Kirchhoff-Institut für Physik, Universität Heidelberg, Heidelberg, Germany^a*

¹⁵ *Institut für experimentelle und Angewandte Physik, Universität Kiel, Kiel, Germany*

¹⁶ *Institute of Experimental Physics, Slovak Academy of Sciences, Košice, Slovak Republic^{e,f}*

¹⁷ *School of Physics and Chemistry, University of Lancaster, Lancaster, UK^b*

¹⁸ *Department of Physics, University of Liverpool, Liverpool, UK^b*

¹⁹ *Queen Mary and Westfield College, London, UK^b*

²⁰ *Physics Department, University of Lund, Lund, Sweden^g*

²¹ *Physics Department, University of Manchester, Manchester, UK^b*

²² *CPPM, CNRS/IN2P3 - Univ Mediterranee, Marseille - France*

²³ *Institute for Theoretical and Experimental Physics, Moscow, Russia^l*

²⁴ *Lebedev Physical Institute, Moscow, Russia^e*

²⁵ *Max-Planck-Institut für Physik, München, Germany*

²⁶ *LAL, Université de Paris-Sud, IN2P3-CNRS, Orsay, France*

²⁷ *LPNHE, Ecole Polytechnique, IN2P3-CNRS, Palaiseau, France*

²⁸ *LPNHE, Universités Paris VI and VII, IN2P3-CNRS, Paris, France*

²⁹ *Institute of Physics, Academy of Sciences of the Czech Republic, Praha, Czech Republic^{e,i}*

³⁰ *Faculty of Mathematics and Physics, Charles University, Praha, Czech Republic^{e,i}*

³¹ *Dipartimento di Fisica Università di Roma Tre and INFN Roma 3, Roma, Italy*

³² *Paul Scherrer Institut, Villigen, Switzerland*

³³ *Fachbereich Physik, Bergische Universität Gesamthochschule Wuppertal, Wuppertal, Germany*

³⁴ *Yerevan Physics Institute, Yerevan, Armenia*

³⁵ *DESY, Zeuthen, Germany*

³⁶ *Institut für Teilchenphysik, ETH, Zürich, Switzerland^j*

³⁷ *Physik-Institut der Universität Zürich, Zürich, Switzerland^j*

³⁸ *Also at Physics Department, National Technical University, Zografou Campus, GR-15773 Athens, Greece*

- ³⁹ Also at Rechenzentrum, Bergische Universität Gesamthochschule Wuppertal, Germany
⁴⁰ Also at Institut für Experimentelle Kernphysik, Universität Karlsruhe, Karlsruhe, Germany
⁴¹ Also at Dept. Fis. Ap. CINVESTAV, Mérida, Yucatán, México^k
⁴² Also at University of P.J. Šafárik, Košice, Slovak Republic
⁴³ Also at CERN, Geneva, Switzerland
⁴⁴ Also at Dept. Fis. CINVESTAV, México City, México^k

^a Supported by the Bundesministerium für Bildung und Forschung, FRG, under contract numbers 05 H1 1GUA /1, 05 H1 1PAA /1, 05 H1 1PAB /9, 05 H1 1PEA /6, 05 H1 1VHA /7 and 05 H1 1VHB /5

^b Supported by the UK Particle Physics and Astronomy Research Council, and formerly by the UK Science and Engineering Research Council

^c Supported by FNRS-FWO-Vlaanderen, IISN-IIKW and IWT

^d Partially Supported by the Polish State Committee for Scientific Research, grant no. 2P0310318 and SPUB/DESY/P03/DZ-1/99 and by the German Bundesministerium für Bildung und Forschung

^e Supported by the Deutsche Forschungsgemeinschaft

^f Supported by VEGA SR grant no. 2/1169/2001

^g Supported by the Swedish Natural Science Research Council

ⁱ Supported by the Ministry of Education of the Czech Republic under the projects INGO-LA116/2000 and LN00A006, by GAUK grant no 173/2000

^j Supported by the Swiss National Science Foundation

^k Supported by CONACyT

^l Partially Supported by Russian Foundation for Basic Research, grant no. 00-15-96584

[†] Deceased

1 Introduction

In this paper we describe the first measurement of multi–electron production at high transverse momentum (P_T) in electron¹–proton interactions at HERA. Within the Standard Model (SM), the production of multi–lepton events in ep collisions proceeds mainly through photon–photon interactions; photons radiated from the incident electron and proton interact to produce a pair of leptons, $\gamma\gamma \rightarrow \ell^+\ell^-$ [1]. At large invariant masses, multi–lepton production may be sensitive to new phenomena, for instance the production of a doubly charged Higgs boson [2] or processes involving bileptons, generic bosons carrying two units of lepton number [3].

The analysis presented here is based on data recorded in 1994–2000 by the H1 experiment. Electrons of 27.6 GeV collided with protons of 820 or 920 GeV, corresponding to centre–of–mass energies \sqrt{s} of 301 GeV or 319 GeV, respectively. The total integrated luminosity of 115.2 pb^{-1} consists of 36.5 pb^{-1} of e^+p collisions recorded at $\sqrt{s} = 301 \text{ GeV}$ and 65.1 pb^{-1} recorded at 319 GeV, as well as 13.6 pb^{-1} of e^-p collisions recorded at $\sqrt{s} = 319 \text{ GeV}$. A related study of muon pair production is presented in [4].

2 Standard Model Processes and their Simulation

The main SM processes contributing to multi–electron production at HERA are summarised in figure 1. The dominant contribution, shown in diagram 1a, is due to electron pair production through the interaction of two photons radiated from the incident electron and proton. Electron pairs can also originate from internal conversion of a photon (γ) or a Z^0 boson, radiated either from the electron line (diagram 1b) or from the quark line (diagram 1c). The pole due to the electron propagator in diagrams 1a and 1b corresponds to an e^+e^- interaction in which one of the electrons is emitted from a photon radiated from the proton. This mechanism is called the Cabibbo–Parisi process. Its contribution is one order of magnitude lower than the photon–photon contribution, except at high transverse momentum, where it is more significant due to s -channel Z^0 boson production (diagram 1b). In diagram 1c, the pole due to the quark propagator corresponds to the Drell–Yan process, $q\bar{q} \rightarrow e^+e^-$. Its contribution is small compared with the photon–photon and Cabibbo–Parisi processes [5].

If the photon coupled to the incoming electron has a high virtuality, the incident electron can scatter through a large angle and with high transverse momentum. If the scattered electron is observed in the detector, it is indistinguishable from the pair–produced electron of the same charge.

The Monte Carlo generator GRAPE [6] simulates lepton pair production in ep collisions using the full set of electroweak matrix elements at the tree level, with the exception of the Drell–Yan pole contribution. GRAPE is based on the automatic Feynman graphs calculation program GRACE [7]. Initial and final state radiation processes (QED and QCD parton showers) are simulated in the leading log approximation. The production of τ lepton pairs and their subsequent electronic decay is also simulated with GRAPE and composes about 2% of the multi–electron event sample. The Drell–Yan contribution is simulated using the PYTHIA [8]

¹In this paper the term “electron” is used generically to refer to both electrons and positrons.

event generator. Its contribution is found to be very small in the phase space relevant here and is neglected in the following.

In GRAPE the proton interaction is divided into in three phase space regions: elastic, quasi-elastic and inelastic. In the case of elastic scattering, $ep \rightarrow ee^+e^-p$, the proton vertex is described in terms of dipole form factors. The quasi-elastic domain is defined by requiring that the mass of the hadronic final state $M_X < 5$ GeV or that the virtuality of the photon coupled to the proton $Q_p^2 < 1$ GeV². In the region $M_X < 2$ GeV a resonance parameterisation [9] is used for the proton vertex. In the remaining quasi-elastic phase space, a fit to photoproduction and deep inelastic scattering data is used [10]. The inelastic regime corresponds to electron-quark interactions with $M_X > 5$ GeV and $Q_p^2 > 1$ GeV². In this case, the proton structure is parameterised using the CTEQ5L parton distributions [11]. The fragmentation and hadronisation processes are simulated using the SOPHIA program [12] in the quasi-elastic and PYTHIA [8] in the inelastic regime.

The uncertainty attributed to the GRAPE calculation in this analysis is 3%. This value results mainly from the uncertainties in the QED matrix element calculation (1%), the parameterisation of the structure functions and the phase space separation between quasi-elastic and inelastic processes.

The GRAPE prediction is cross-checked using the LPAIR generator [13], which contains only the photon-photon process. When restricted to this process, the total and differential cross sections produced with LPAIR and GRAPE agree at the percent level. The additional diagrams in GRAPE increase the predicted cross section by 10 % on average in the phase space considered here. The increase is more pronounced (up to 30 %) for di-lepton masses which are either very low (photon internal conversions) or around 90 GeV (Z^0 resonance production).

The main experimental backgrounds to multi-electron production are processes in which, in addition to a true electron, one or more fake electrons are reconstructed in the final state. The dominant contribution arises from neutral current Deep Inelastic Scattering (DIS) events ($ep \rightarrow eX$) in which, in addition to the scattered electron, hadrons or radiated photons are incorrectly identified as electrons. QED Compton scattering ($ep \rightarrow e\gamma X$) can also contribute if the photon is misidentified as an electron. The DIS and elastic Compton processes are simulated using the DJANGO [14] and WABGEN [15] generators, respectively.

All generated events are passed through the full GEANT [16] based simulation of the H1 apparatus and are reconstructed using the same program chain as for the data.

3 Experimental Conditions

A detailed description of the H1 detector can be found in [17]. The components essential for this analysis are described briefly here.

A tracking system consisting of central and forward² drift chambers is used to measure charged particle trajectories and to determine the interaction vertex. The central tracker is composed of two concentric cylindrical drift chambers with an active detection region starting at a

²The origin of the H1 coordinate system is the nominal ep interaction point. The direction of the proton beam defines the positive z -axis (forward direction). Transverse momenta are measured in the x - y plane. Polar (θ) and azimuthal (ϕ) angles are measured with respect to this reference system. The pseudorapidity is defined as $\eta = -\log \tan(\theta/2)$.

radius of 22 cm. The angular range $37^\circ < \theta < 144^\circ$ is covered by both chambers. The inner drift chamber provides full acceptance for particles in the range $22^\circ < \theta < 159^\circ$. Particles at $\theta = 20^\circ$ cross 83% of its acceptance region. Transverse momenta (P_T) are determined from the curvature of the particle trajectories in a magnetic field of 1.15 Tesla. The central tracking system provides transverse momentum measurements with a resolution of $\sigma_{P_T}/P_T^2 = 5 \times 10^{-3} \text{ GeV}^{-1}$. The tracking is complemented in the region $7^\circ < \theta < 25^\circ$ by a system of drift chambers perpendicular to the beam axis.

Hadronic and electromagnetic final state particles are absorbed in a highly segmented liquid argon calorimeter [18] covering the range $4^\circ < \theta < 153^\circ$. The calorimeter is 5 to 8 hadronic interaction lengths deep, depending on the polar angle and has an electromagnetic section which is 20 to 30 radiation lengths deep. Electromagnetic shower energies are measured with a precision of $\sigma(E)/E = 12\%/\sqrt{E/\text{GeV}} \oplus 1\%$ and hadronic shower energies with a precision of $\sigma(E)/E = 50\%/\sqrt{E/\text{GeV}} \oplus 2\%$, as measured in test beams [19]. The electromagnetic energy scale is known to 0.7% in the central region and to 3% in the forward region. The hadronic energy scale is known to 2%.

In the backward region, energy measurements are provided by a lead/scintillating-fibre calorimeter³ [20] covering the range $155^\circ < \theta < 178^\circ$. The calorimeter system is surrounded by a superconducting coil with an iron yoke which is instrumented with streamer tubes. The electron and photon taggers located downstream of the interaction point in the electron beam direction are used to determine the luminosity through the measurement of the Bethe-Heitler $ep \rightarrow e\gamma p$ process.

The trigger used relies on the liquid argon calorimeter signals and has an efficiency which is greater than 95% for events in which an electron of energy above 10 GeV is detected.

4 Data Analysis

4.1 Multi-electron event selection

The multi-electron event selection is based on a procedure which is designed to minimise the contribution of fake electrons, while keeping a high efficiency for identifying true electrons and allowing reliable monitoring of the overall selection efficiency.

As a first step, electron candidates with energies above 5 GeV are identified in the liquid argon and backward calorimeters, in the range $5^\circ < \theta < 175^\circ$. Electromagnetic showers are identified with an efficiency of better than 98% using pattern recognition algorithms based on the geometric profiles expected for electrons. The remaining calorimeter clusters are attributed to hadronic activity and are combined into jets using an inclusive k_T algorithm [21], with a minimum jet transverse momentum of 4 GeV. Electron candidates are required to be isolated by demanding that they are separated from other electrons or jets by at least 0.5 units in the $\eta - \phi$ plane. In addition, the total hadronic energy within 0.75 units in $\eta - \phi$ of the electron direction is required to be below 2.5% of the electron energy.

³This device was installed in 1995, replacing a lead-scintillator “sandwich” calorimeter [17].

In the region of angular overlap between the liquid argon calorimeter and the central drift chambers ($20^\circ < \theta < 150^\circ$), the calorimetric electron identification is complemented by tracking conditions. In this region it is required that a high quality track be geometrically matched to the electromagnetic cluster with a distance of closest approach to the cluster centre of gravity of less than 12 cm. The starting radius of the measured track, defined as the distance between the first measured point in the central drift chambers and the beam axis, is required to be below 30 cm in order to reject photons that convert in the central tracker material beyond this radius. The transverse momentum of the associated track $P_T^{e_{tk}}$ and the calorimetric transverse momentum P_T^e are required to satisfy the condition $1/P_T^{e_{tk}} - 1/P_T^e < 0.02 \text{ GeV}^{-1}$. No other high quality track is allowed within 0.5 units in $\eta - \phi$ of the electron direction. These additional constraints strongly reduce the contribution of fake electrons from misidentified photons and hadrons. The resulting electron finding efficiency is 88%. Electrons selected in this polar angular range are called “central electrons” hereinafter.

Due to the higher material density in the forward region ($5^\circ < \theta < 20^\circ$) the electrons are more likely to shower and therefore no track conditions are required. The same applies in the backward region ($150^\circ < \theta < 175^\circ$). The forward electron energy threshold is raised to 10 GeV in order to reduce the number of fake electrons arising from hadrons in DIS events.

The final multi–electron event selection requires that there be two central electron candidates, of which one must have $P_T^e > 10 \text{ GeV}$ and the other $P_T^e > 5 \text{ GeV}$. Additional electron candidates are identified in the central and backward regions with $E^e > 5 \text{ GeV}$ and in the forward region with $E^e > 10 \text{ GeV}$. The electron candidates are ordered according to decreasing P_T , $P_T^{e_i} > P_T^{e_{i+1}}$.

The selected events are classified as “2e” if only the two central electron candidates are identified and “3e” if exactly one additional electron candidate is identified. A subsample of the “2e” sample, labelled “ $\gamma\gamma$ ”, is selected in order to measure the pair production cross section in a well defined phase space region dominated by photon–photon collisions with low background. In this subsample, the two electrons must be of opposite charge and a significant deficit compared to the initial state must be observed in the difference $E - P_z$ of the energy and longitudinal momentum of all visible particles ($E - P_z < 45 \text{ GeV}$)⁴. These two conditions ensure that the incident electron is lost in the beam pipe after radiating a quasi–real photon of squared four–momentum Q^2 lower than 1 GeV^2 .

4.2 Background studies

DIS and Compton processes can contribute to the selected multi–electron sample if a photon or a particle from the hadronic final state is misidentified as an electron. In order to quantify the uncertainty on the background prediction and test the performance and reliability of the electron identification procedure, several samples in which these background processes are enhanced are studied.

⁴For fully contained events or events where only longitudinal momentum along the proton direction (+z) is undetected, one expects $E - P_z = 2E_e^0 = 55.2 \text{ GeV}$, where E_e^0 is the energy of the incident electron. If the scattered electron is undetected, the threshold $E - P_z < 45 \text{ GeV}$ corresponds to a cut on the fractional energy loss $y = (E - P_z)/2E_e^0 < 0.82$.

- Electron misidentification in the central region is investigated by measuring the probability of selecting a second electron in addition to the scattered electron in DIS candidate events when the track quality criteria are relaxed. From a sample of 244980 DIS candidates, 1563 events with a second electromagnetic central cluster are selected if no tracking conditions are applied to this cluster. The fake electrons are predominantly photons from DIS or Compton events (figure 2a). This contribution is greatly reduced by requiring a geometrical track–cluster match (figure 2b). The remaining sample consists of 250 events. The fake electron background is described by the simulation at the 20% level.
- Electron misidentification in the forward region affects only the “3e” selection. The dominant contribution to this background is the misidentification of a hadron as an electron. The fake electron background in this region is studied with the DIS event sample in an analysis similar to that described above. Fake electrons in the forward region are also searched for in an inelastic Compton event sample with one electron and one photon in the central region. The fake electron background in the forward region is described by the simulation at the 20% level.
- Detailed studies of photon conversions are performed using a sample enriched with elastic Compton events, selected by requiring one central electron plus a second central electromagnetic cluster (photon candidate) and no significant additional energy in the calorimeters. Distributions of the charged tracks associated with the photon candidate are shown in figures 2c and 2d. The number of tracks (figure 2c) and their starting radius (figure 2d) are well reproduced by the simulation. In figure 2d, the central tracker structure is visible as peaks in the distribution, corresponding to photon conversions in the tracker walls. The first peak is populated by tracks associated with true electrons and by tracks from conversions which occur before the active tracker volume. The second peak is due to photon conversions in the dead material between the inner and outer central trackers. These conversions are described by the simulation to better than 20%.

Based on those studies, the uncertainty on the background simulation is estimated to be 20%.

4.3 Systematic uncertainties

The systematic uncertainties are related to the measurement of the electron pair production process, to the theoretical description of this process and to the background simulation.

The main measurement uncertainty is due to the tracking conditions in the electron identification procedure. The electron track association efficiency is measured with a DIS sample selected with $E - P_z > 45$ GeV and a single electromagnetic cluster in the calorimeter with a transverse momentum above 10 GeV in the polar angle interval $20^\circ < \theta < 150^\circ$. The measured average track association efficiency is 90% and varies only slightly with the track momentum and polar angle. This efficiency, measured to a precision ranging from 3% for polar angles around 90° to 15% at the forward edge of the angular acceptance of the central tracker ($\theta = 20^\circ$), is well described by the simulation. Uncertainties on the energy scales of the calorimeters, on the trigger efficiency and on the luminosity measurement are also taken into account. The total measurement uncertainty is typically 7% for the “2e” selection and 10% for the “3e” selection.

The theoretical uncertainty on the pair production process cross section, calculated with GRAPE, is 3%, as explained in section 2. The uncertainty on the Compton and DIS background contributions is 20%, deduced from the studies presented in section 4.2.

The error on the event yields predicted by GRAPE (section 5.1) contains all measurement and theoretical errors added in quadrature. The uncertainty on the total SM prediction also includes the errors on the Compton and DIS backgrounds.

The error on the extracted cross sections (section 5.2) includes all measurement and background errors as described above. Theoretical errors are applied to the GRAPE prediction of the cross sections.

5 Results

5.1 Multi-electron event samples

The multi-electron event yields are summarised in table 1. The observed numbers of “2e” and “3e” events are in agreement with the expectations, as is the number of events in the “ $\gamma\gamma$ ” sample. No event is found with four or more identified electrons.

The distributions of longitudinal momentum balance $E - P_z$, missing transverse momentum P_T^{miss} and hadronic transverse momentum $P_T^{hadrons}$ are presented in figure 3. The “3e” events accumulate at $E - P_z$ values around 55 GeV, as expected if the scattered electron is visible in the detector. The “2e” events show a tail at lower $E - P_z$, due to the scattered electron being lost in the beam pipe, corresponding to the dominant $\gamma\gamma$ topology. The missing transverse momentum P_T^{miss} is taken to be the modulus of the vector sum of the transverse momenta of all visible particles. The P_T^{miss} distributions are consistent with the expectation for no emission of undetected particles with substantial transverse momentum. The spectrum of the transverse momentum $P_T^{hadrons}$ of all visible particles except identified electrons is also well described by the SM prediction.

The distributions of the individual electron transverse momenta $P_T^{e_i}$ are steeply falling as shown in figure 4. The “2e” and “3e” samples are in good overall agreement with the SM, except for three “2e” events with $P_T^{e_1}$ above 50 GeV, where the SM expectation is small.

The distribution of the invariant mass of the two highest P_T electrons in the event (M_{12}) and the correlation with the scalar sum $P_T^{e_1} + P_T^{e_2}$ are shown in figure 5. The agreement with the SM prediction is good at low M_{12} . However, three “2e” and three “3e” events are seen with invariant masses M_{12} above 100 GeV, where the SM expectation is small. The three “2e” events are the same as those observed at high $P_T^{e_1}$. The invariant masses M_{13} , M_{23} and M_{123} of the other possible electron combinations in the “3e” sample are shown in figure 6. No event is seen with an unexpectedly high M_{13} or M_{23} . The three high M_{12} events also give rise to the largest tri-electron masses M_{123} . The comparison of the observed events with masses M_{12} above 100 GeV with the SM expectations is presented in table 2. These events are discussed in detail in section 5.3.

5.2 Cross section measurement

Using the selected “ $\gamma\gamma$ ” sample, electron pair production cross sections are measured in the kinematic region defined by

$$20^\circ < \theta^{e_{1,2}} < 150^\circ, \quad P_T^{e_1} > 10 \text{ GeV}, \quad P_T^{e_2} > 5 \text{ GeV}, \quad y < 0.82, \quad Q^2 < 1 \text{ GeV}^2.$$

For this measurement, the data samples collected at $\sqrt{s}=301 \text{ GeV}$ and 319 GeV are combined taking into account their respective luminosities. Assuming a linear dependence of the cross section on the proton beam energy, as predicted by the SM, the resulting cross section corresponds to an effective $\sqrt{s} = 313 \text{ GeV}$.

After background subtraction, the observed number of events is corrected for acceptance and detector effects to obtain the cross section. The generator GRAPE is used to calculate the detector acceptance A for this region of phase space. The acceptance accounts for detection efficiencies and migrations. The cross section is thus

$$\sigma = \frac{N_{\text{data}} - N_{\text{bgd}}}{\mathcal{L}A},$$

where N_{data} is the number of events observed, N_{bgd} is the number of events expected from background processes (DIS and Compton) and \mathcal{L} is the integrated luminosity of the data sample.

The $ep \rightarrow ee^+e^-X$ cross section, integrated over the phase space defined above, is

$$\sigma = (0.59 \pm 0.08 \pm 0.05) \text{ pb},$$

where the first error is statistical and the second systematic, obtained as described in section 4.2. This result agrees well with the SM expectation of $(0.62 \pm 0.02) \text{ pb}$, calculated with GRAPE. The differential cross sections as a function of $P_T^{e_1}$, M_{12} and P_T^{hadrons} are shown in figure 7 and table 3. The measurements are in good agreement with the expected cross sections.

5.3 Discussion of high mass events

All six events with $M_{12} > 100 \text{ GeV}$ were recorded during positron–proton collisions. For these events, displayed in figure 8, all available detector information supports the interpretation of the electron candidates as being true electrons. The electromagnetic shower shapes are checked individually and found to be similar to those expected from the calorimeter response to electrons. All central tracks yield a specific ionisation in the central drift chamber as expected for single electrons. The measurements of the central electron momenta by the tracker and the calorimeter are compatible within errors. The forward electron candidates in the “3e” events 4, 5 and 6 all have at least one track pointing to the calorimetric energy cluster, although no such requirement is made in the identification procedure.

Although classified as “2e”, event 1 also contains a third electron candidate with energy below the identification threshold. Similarly, event 3 has a compact electromagnetic energy deposit located at the forward boundary of the liquid argon calorimeter, outside the electron identification fiducial volume. This event also contains a low energy converted photon radiated

close to electron e_2 . With the exception of event 6, which has a high energy forward hadronic jet, the events show no hadronic activity in the detector. It should be noted that the high mass di–electron topology differs for the observed events classified as “2e” and “3e”. In the former case, the high–mass is formed from two central high– P_T electrons, whereas in the latter it is formed from one forward and one central electron, both of intermediate P_T (figure 5).

The event kinematics of the six high mass events are presented in table 4. The electron energy, electron polar angle and forward and backward electron azimuthal angles are measured from the calorimetric deposits. For the central electrons, the azimuthal angle is measured from the associated track, which yields a better precision. The electric charge of the electrons, measured in the central region from the associated track curvature, is given in table 4 if the significance of its determination exceeds two standard deviations. All events are compatible with the presence of one e^- and two e^+ in the final state, as expected from pair production process.

Imposing longitudinal and transverse momentum conservation, a constrained fit can be performed to improve the kinematic measurement. This corresponds to an adjustment of particle observables (energy, polar and azimuthal angles) within experimental errors in order to achieve $E - P_z = 55.2$ GeV and $P_T^{miss} = 0$ GeV. In event 2 only two electrons are visible and the measured $E - P_z$ value is significantly lower than 55 GeV. For this event it is supposed that the scattered electron has escaped down the beampipe and therefore the $E - P_z$ constraint is removed in the kinematic fit. The M_{12} values obtained from the kinematic fit are indicated in table 4. They are consistent with the direct measurements. The errors are reduced by more than a factor of two with the exception of event 2. The χ^2 per degree of freedom of the kinematic fit is in the range 0.7 to 1.7 for the six events, showing that the kinematics of the six high mass events are well understood within the measurement errors. The M_{12} values are incompatible with the interpretation of the six high mass electron pairs as the decay of a single narrow resonance. The same is true for the M_{123} values in the “3e” high mass events.

6 Summary

High– P_T multi–electron production is measured for the first time in ep scattering at HERA. The di–electron and tri–electron event yields are in good overall agreement with the SM predictions. No events are observed with more than three identified electrons, again in agreement with the SM expectation. Differential cross sections for electron pair production are extracted in a restricted phase space region dominated by photon–photon interactions and are found to agree with the predictions.

Within the di– and tri–electron samples, the invariant mass of the two electrons with the highest transverse momenta is studied. For masses above 100 GeV, three events classified as di–electrons and three events classified as tri–electrons are observed, compared to SM expectations of 0.30 ± 0.04 and 0.23 ± 0.04 , respectively.

Acknowledgements

We are grateful to the HERA machine group whose outstanding efforts have made and continue to make this experiment possible. We thank the engineers and technicians for their work in

constructing and maintaining the H1 detector, our funding agencies for financial support, the DESY technical staff for continual assistance, and the DESY directorate for support and the hospitality which they extend to the non-DESY members of the collaboration. The authors wish to thank J. A. M. Vermaseren and T. Abe for many useful discussions.

References

- [1] J. A. M. Vermaseren, Nucl. Phys. B **229** (1983) 347.
- [2] E. Accomando and S. Petrarca, Phys. Lett. B **323** (1994) 212 [hep-ph/9401242].
- [3] F. Cuypers and S. Davidson, Eur. Phys. J. C **2** (1998) 503 [hep-ph/9609487].
- [4] A. Aktas *et al.* [H1 Collaboration], in preparation.
- [5] N. Arteaga-Romero, C. Carimalo and P. Kessler, Z. Phys. C **52** (1991) 289.
- [6] T. Abe, Comput. Phys. Commun. **136** (2001) 126 [hep-ph/0012029].
- [7] T. Ishikawa *et al.* [MINAMI-TATEYA group Collaboration], KEK-92-19.
- [8] PYTHIA 5.7; T. Sjöstrand, CERN-TH-6488 (1992), Comp. Phys. Comm. **82** (1994) 74.
- [9] F. W. Brasse *et al.*, Nucl. Phys. B **110** (1976) 413.
- [10] H. Abramowicz and A. Levy, [hep-ph/9712415].
- [11] H. L. Lai *et al.* [CTEQ Collaboration], Eur. Phys. J. C **12** (2000) 375 [hep-ph/9903282].
- [12] A. Mucke *et al.*, Comp. Phys. Comm. **124** (2000) 290 [astro-ph/9903478].
- [13] LPAIR; S. P. Baranov, O. Dünger, H. Shooshtari and J. A. Vermaseren, Proc. of the Workshop “Physics at HERA” (1991), Eds. W. Buchmüller and G. Ingelman, Vol. 3, p. 1478.
- [14] DJANGO 2.1; G.A. Schuler and H. Spiesberger, Proc. of the Workshop “Physics at HERA” (1991), Eds. W. Buchmüller and G. Ingelman, Vol. 3, p. 1419.
- [15] WABGEN; C. Berger and P. Kandel, Proc. of the Workshop “Monte Carlo Generators for HERA Physics” (1998/1999), DESY-PROC-1999-02, p. 596.
- [16] GEANT3; R. Brun *et al.*, CERN-DD/EE/84-1.
- [17] I. Abt *et al.* [H1 Collaboration], Nucl. Instrum. Meth. A **386** (1997) 310;
I. Abt *et al.* [H1 Collaboration], Nucl. Instrum. Meth. A **386** (1997) 348.
- [18] B. Andrieu *et al.* [H1 Calorimeter Group], Nucl. Instrum. Meth. A **336** (1993) 460.
- [19] B. Andrieu *et al.* [H1 Calorimeter Group], Nucl. Instrum. Meth. A **344** (1994) 492; *idem*,
Nucl. Instrum. Meth. A **350** (1994) 57; *idem*, Nucl. Instrum. Meth. A **336** (1993) 499.
- [20] R. D. Appuhn *et al.* [H1 SPACAL Group], Nucl. Instrum. Meth. A **386** (1997) 397.

- [21] S. D. Ellis and D. E. Soper, Phys. Rev. D **48** (1993) 3160 [hep-ph/9305266];
C. Adloff *et al.* [H1 Collaboration], Nucl. Phys. B **545** (1999) 3 [hep-ex/9901010].

Selection	Data	SM	Pair Production (GRAPE)	DIS + Compton
“2e”	108	117.1 ± 8.6	91.4 ± 6.9	25.7 ± 5.2
“3e”	17	20.3 ± 2.1	20.2 ± 2.1	0.1 ± 0.1
“4e” or more	0	0.12 ± 0.04	0.12 ± 0.04	< 0.02 (95% C.L.)
“ $\gamma\gamma$ ” subsample	42	44.9 ± 4.2	43.7 ± 4.2	1.2 ± 0.4

Table 1: Observed and predicted multi–electron event yields for the samples described in the text. The analysed data sample corresponds to an integrated luminosity of 115.2 pb^{-1} . The errors on the predictions include model uncertainties and experimental systematic errors added in quadrature.

Selection	Data	SM	Pair Production (GRAPE)	DIS + Compton
“2e” $M_{12} > 100 \text{ GeV}$	3	0.30 ± 0.04	0.21 ± 0.03	0.09 ± 0.02
“3e” $M_{12} > 100 \text{ GeV}$	3	0.23 ± 0.04	0.23 ± 0.03	< 0.02 (95% C.L.)

Table 2: Observed and predicted multi–electron event yields for masses $M_{12} > 100 \text{ GeV}$ for the samples described in the text. The analysed data sample corresponds to an integrated luminosity of 115.2 pb^{-1} . The errors on the predictions include model uncertainties and experimental systematic errors added in quadrature.

Variable range [GeV]	Measured cross section [pb/GeV]	Pair Production (GRAPE) cross section [pb/GeV]
$d\sigma/dP_T^{e_1}$		
$10 < P_T^{e_1} < 15$	$0.092 \pm 0.016 \pm 0.009$	0.090 ± 0.003
$15 < P_T^{e_1} < 20$	$0.021 \pm 0.008 \pm 0.002$	0.023 ± 0.001
$20 < P_T^{e_1} < 25$	$0.0053 \pm 0.0037 \pm 0.0007$	0.0065 ± 0.0002
$d\sigma/dM_{12}$		
$15 < M_{12} < 25$	$0.030 \pm 0.007 \pm 0.003$	0.027 ± 0.001
$25 < M_{12} < 40$	$0.015 \pm 0.004 \pm 0.001$	0.017 ± 0.001
$40 < M_{12} < 60$	$0.0020 \pm 0.0012 \pm 0.0002$	0.0026 ± 0.0001
$d\sigma/dP_T^{hadrons}$		
$0 < P_T^{hadrons} < 5$	$0.079 \pm 0.014 \pm 0.009$	0.087 ± 0.003
$5 < P_T^{hadrons} < 12$	$0.028 \pm 0.011 \pm 0.002$	0.018 ± 0.001
$12 < P_T^{hadrons} < 25$	$0.0032 \pm 0.0023 \pm 0.0005$	0.0041 ± 0.0001

Table 3: Differential cross sections $d\sigma/dP_T^{e_1}$, $d\sigma/dM_{12}$ and $d\sigma/dP_T^{hadrons}$ for the process $ep \rightarrow ee^+e^-X$ in a restricted phase space (see text). The differential cross sections are averaged over the quoted intervals. The first error is statistical and the second is systematic. Theoretical predictions with GRAPE are also shown.

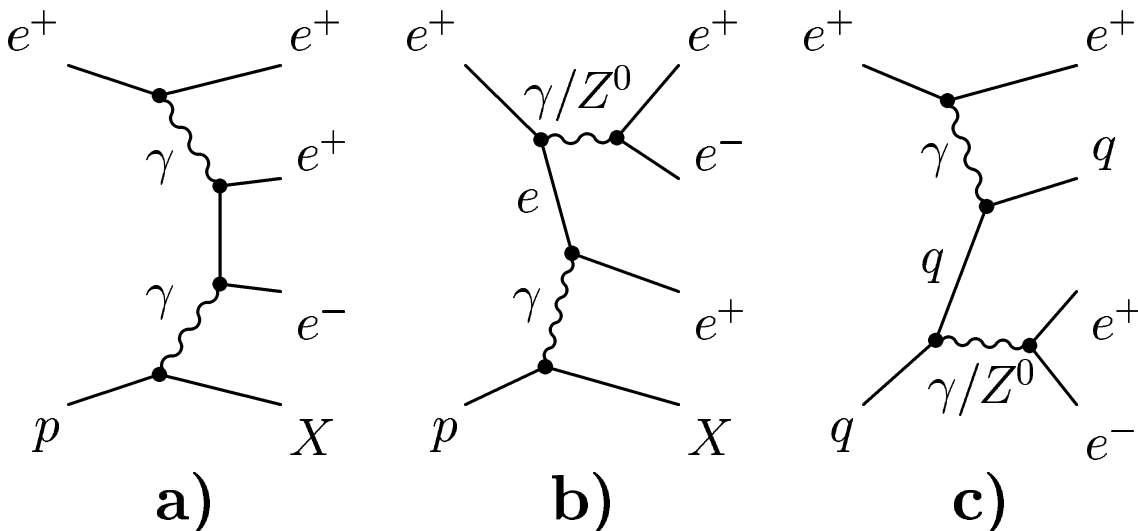


Figure 1: The main processes involved in lepton pair production. Examples of Feynman diagrams are shown for: a) photon-photon interaction; b) and c) γ/Z^0 boson conversion. The hadronic final state (X) can be a proton (elastic process) or a higher mass system (quasi-elastic and inelastic processes).

Particle	E [GeV]	θ [degrees]	ϕ [degrees]	Charge (significance)
Multi-electron Event 1 (2e)				
Run 83507	$E - P_z = 54.0 \pm 1.1$ GeV		$P_T^{miss} = 3.1 \pm 1.8$ GeV	
Event 16817	$M_{12} = 111.2 \pm 2.4$ GeV		$M_{12}^{fit} = 111.3 \pm 0.4$ GeV	
e ₁	90.3 ± 3.1	36.6 ± 0.2	98.48 ± 0.05	- (4σ)
e ₂	53.6 ± 1.4	69.6 ± 0.3	-77.05 ± 0.05	undetermined
low energy e	4.4 ± 0.3	44.3 ± 0.3	-155.46 ± 0.03	+ (70σ)
Multi-electron Event 2 (2e)				
Run 89256	$E - P_z = 43.9 \pm 0.8$ GeV		$P_T^{miss} = 1.9 \pm 1.8$ GeV	
Event 224212	$M_{12} = 130.0 \pm 2.6$ GeV		$M_{12}^{fit} = 129.3 \pm 2.4$ GeV	
e ₁	132.4 ± 4.3	28.6 ± 0.1	8.73 ± 0.06	undetermined
e ₂	82.4 ± 1.8	48.4 ± 0.2	-171.50 ± 0.03	- (6σ)
Multi-electron Event 3 (2e)				
Run 254959	$E - P_z = 57.3 \pm 1.4$ GeV		$P_T^{miss} = 3.5 \pm 2.0$ GeV	
Event 17892	$M_{12} = 112.5 \pm 2.4$ GeV		$M_{12}^{fit} = 109.5 \pm 1.0$ GeV	
e ₁	96.9 ± 3.3	34.6 ± 0.3	52.66 ± 0.02	+ (10σ)
e ₂	46.1 ± 1.1	80.1 ± 0.9	-125.62 ± 0.01	+ (15σ)
fwd em cluster	70_{-2}^{+100} ^a	4.5 ± 0.1	-132.7 ± 1.0	undetermined
photon	1.1 ± 0.1	132.0 ± 5.5	39.8 ± 7.3	0
^a this error includes the uncertainty due to energy loss in the beampipe				
Multi-electron Event 4 (3e)				
Run 168058	$E - P_z = 55.7 \pm 1.4$ GeV		$P_T^{miss} = 1.1 \pm 0.8$ GeV	
Event 42123	$M_{12} = 137.4 \pm 2.9$ GeV		$M_{12}^{fit} = 138.8 \pm 1.2$ GeV	
e ₁	35.8 ± 0.9	115.6 ± 0.9	-5.98 ± 0.02	+ (18σ)
e ₂	173.0 ± 5.5	6.6 ± 0.1	-159.1 ± 0.5	undetermined
e ₃	44.8 ± 1.7	21.8 ± 0.2	139.10 ± 0.03	- (12σ)
Multi-electron Event 5 (3e)				
Run 192864	$E - P_z = 53.8 \pm 1.4$ GeV		$P_T^{miss} = 0.7 \pm 0.6$ GeV	
Event 123614	$M_{12} = 118.1 \pm 2.6$ GeV		$M_{12}^{fit} = 121.9 \pm 0.6$ GeV	
e ₁	138.9 ± 4.5	10.2 ± 0.1	44.1 ± 0.6	undetermined
e ₂	28.1 ± 0.8	134.7 ± 0.3	-95.85 ± 0.01	+ (25σ)
e ₃	35.3 ± 1.5	26.6 ± 0.1	172.71 ± 0.05	+ (5σ)
Multi-electron Event 6 (3e)				
Run 267312	$E - P_z = 57.4 \pm 1.6$ GeV		$P_T^{miss} = 2.4 \pm 0.8$ GeV	
Event 203075	$M_{12} = 134.7 \pm 3.1$ GeV		$M_{12}^{fit} = 132.3 \pm 1.4$ GeV	
e ₁	186.0 ± 5.9	7.11 ± 0.05	-71.3 ± 0.4	undetermined
e ₂	25.5 ± 0.8	148.8 ± 0.2	120.25 ± 0.02	+ (32σ)
e ₃	8.5 ± 0.5	69.7 ± 0.3	164.90 ± 0.01	+ (57σ)
hadrons ^b	123.2 ± 6.7	6.1 ± 1.1	53.5 ± 1.1	
^b mass of the visible hadronic system: 24.0 ± 2.5 GeV				

Table 4: Reconstructed kinematics of the six multi-electron events with $M_{12} > 100$ GeV (see text). E is the particle's energy and θ and ϕ its polar and azimuthal angles, respectively. The charges of the electron candidates are also given, if they are measured with a significance of better than two standard deviations. The six events were recorded in e^+p collisions.

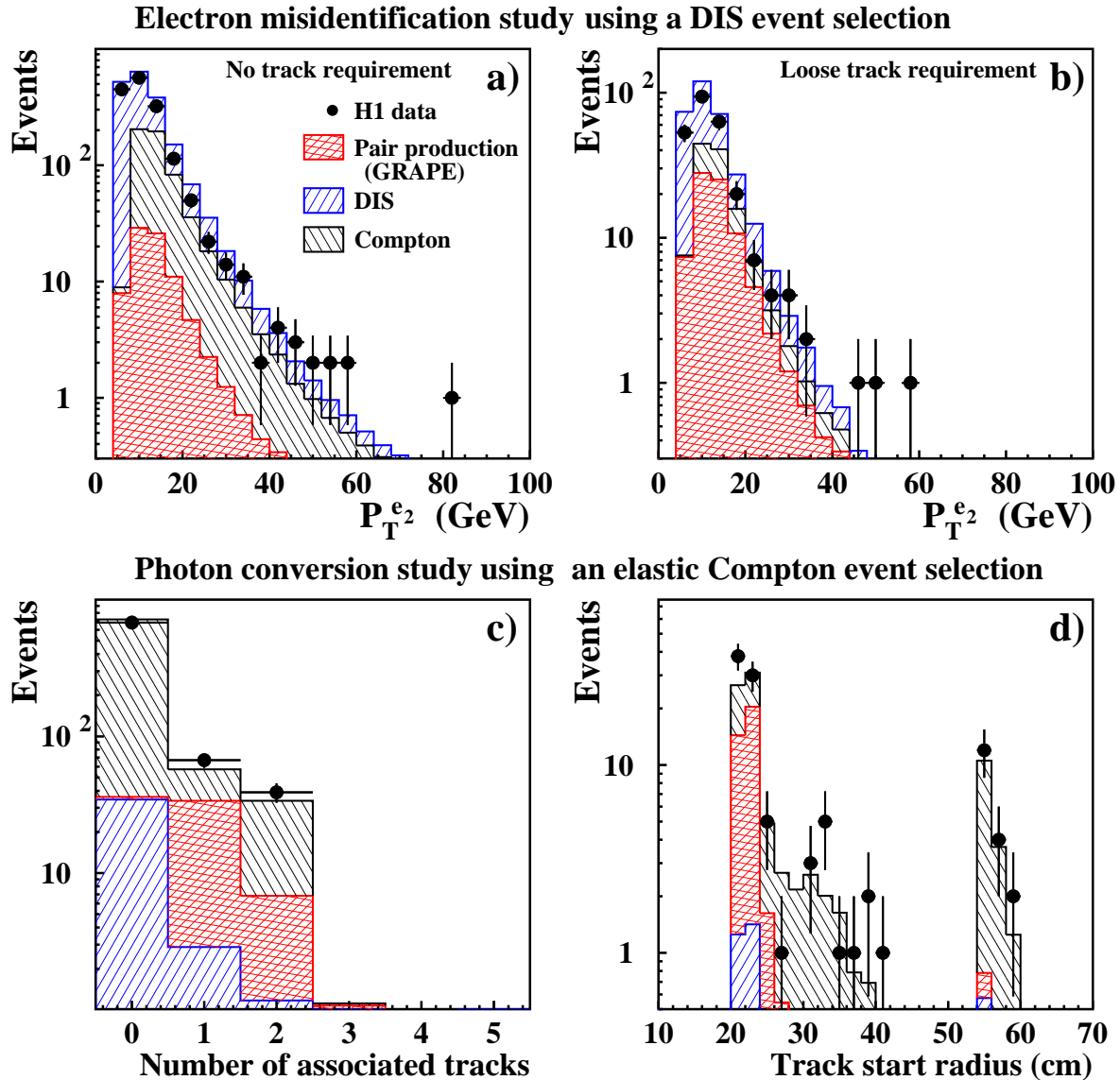


Figure 2: (a and b) Distributions associated with misidentified electrons for a DIS event selection. Transverse momentum spectrum of second electrons identified with either no track requirement (a) or a loose track requirement (b) compared with expectations. (c and d) Study of photon conversions using an elastic Compton event selection: number (c) and starting radius (d) of the tracks associated with the photon candidates compared with expectations.

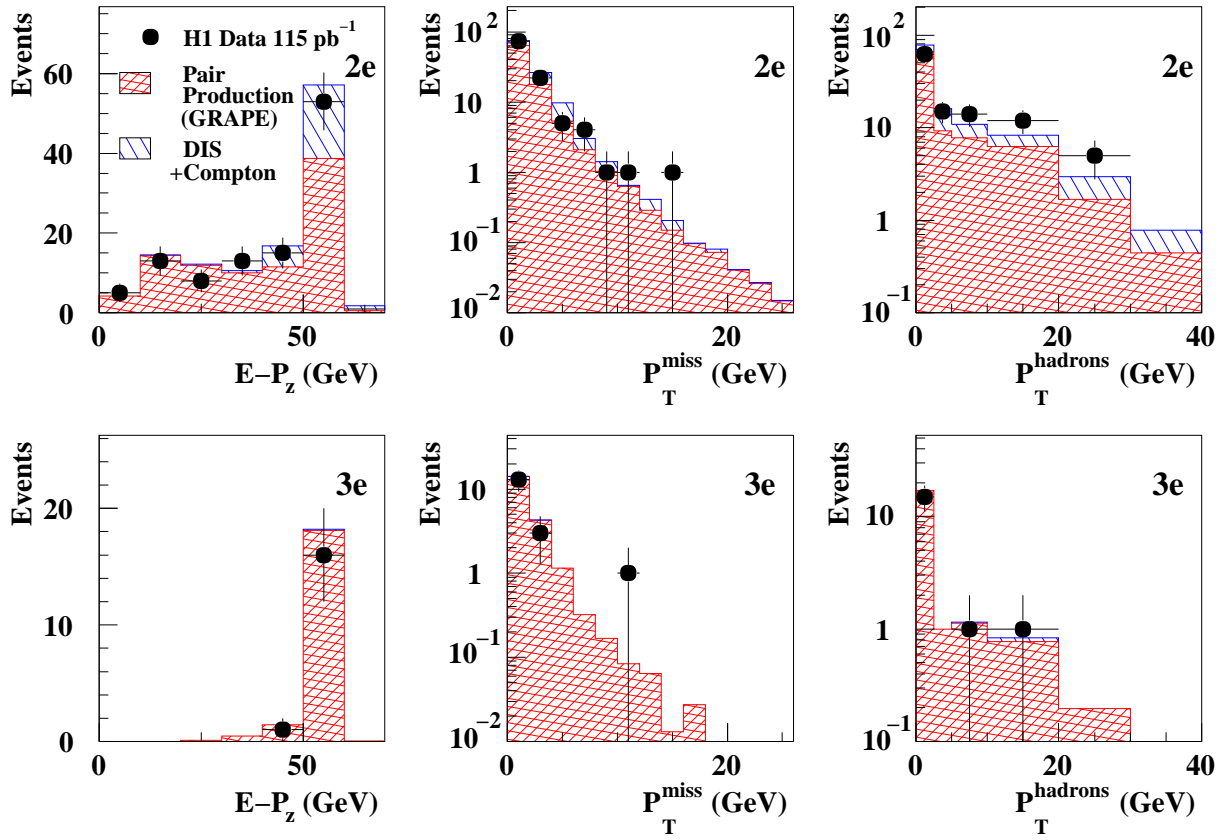


Figure 3: Distributions of $E - P_z$, P_T^{miss} and $P_T^{hadrons}$ for events classified as “2e” (top) and “3e” (bottom), compared with expectations.

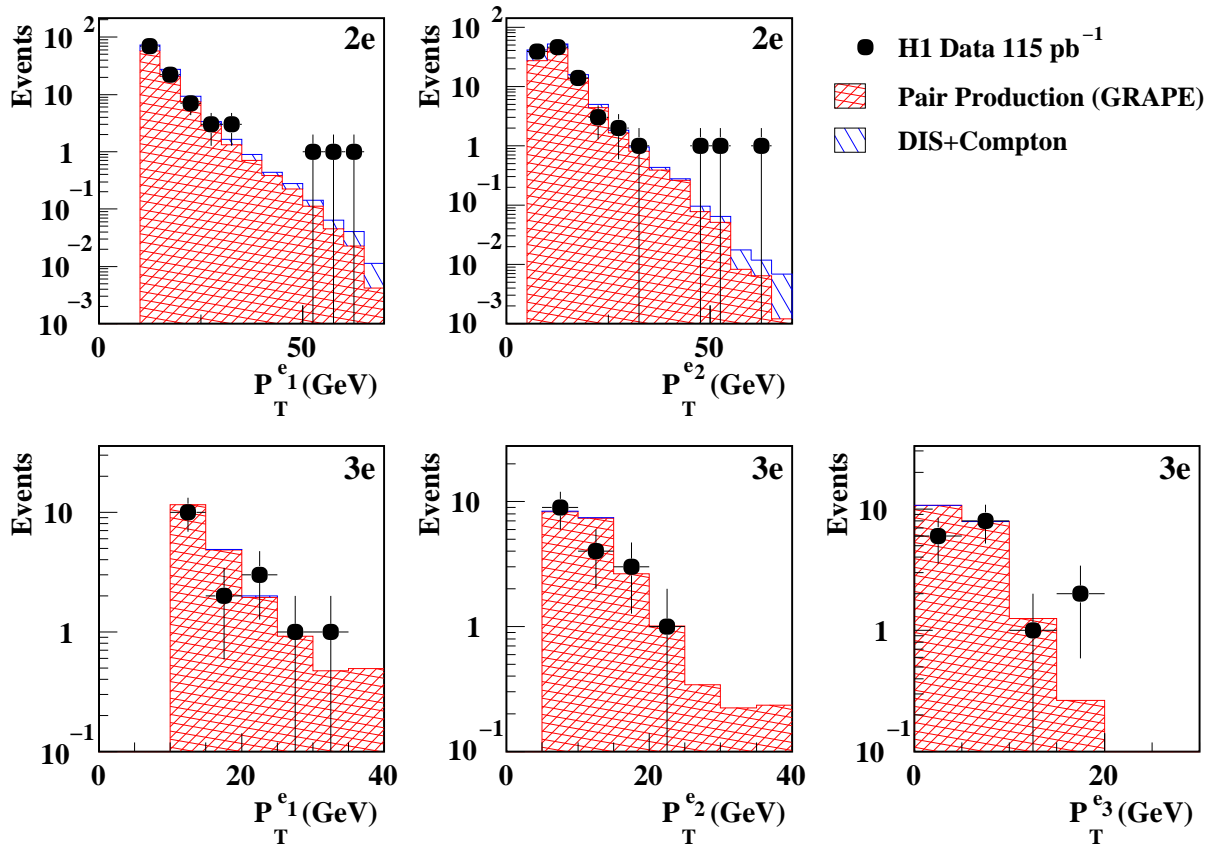


Figure 4: Electron transverse momentum distributions for events classified as “2e” (top) and “3e” (bottom) compared with expectations. Electrons are ordered according to decreasing transverse momentum, $P_T^{e_i} > P_T^{e_{i+1}}$.

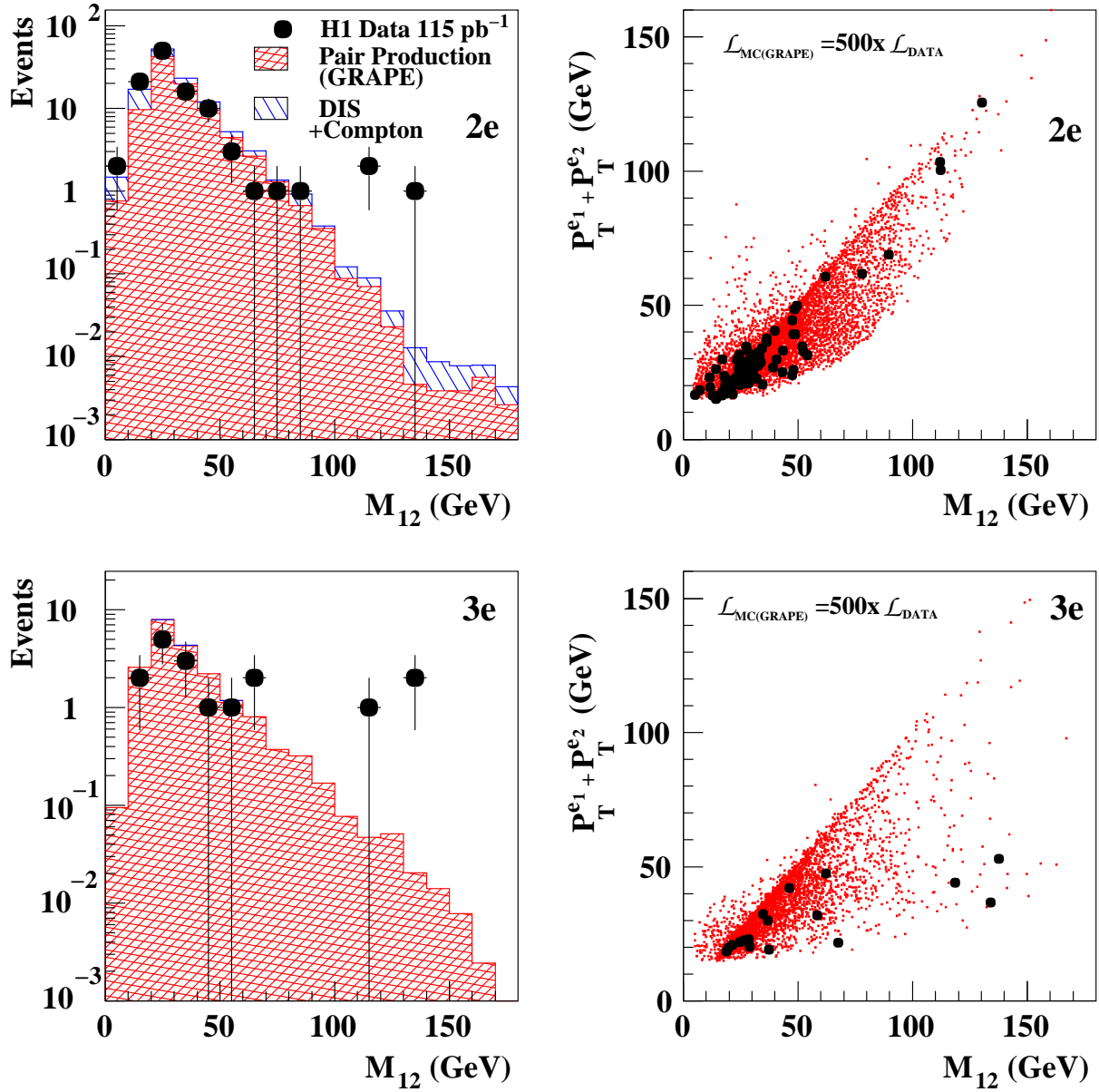


Figure 5: Distribution of the invariant mass M_{12} of the two highest P_T electrons compared with expectations (left) and the correlation of M_{12} with the scalar sum of the P_T 's of the electrons (right) for events classified as "2e" (top) and "3e" (bottom). The bold dots on the right plots represent the data while the small points represent the pair production (GRAPE) prediction for a luminosity 500 times higher than that of the data.

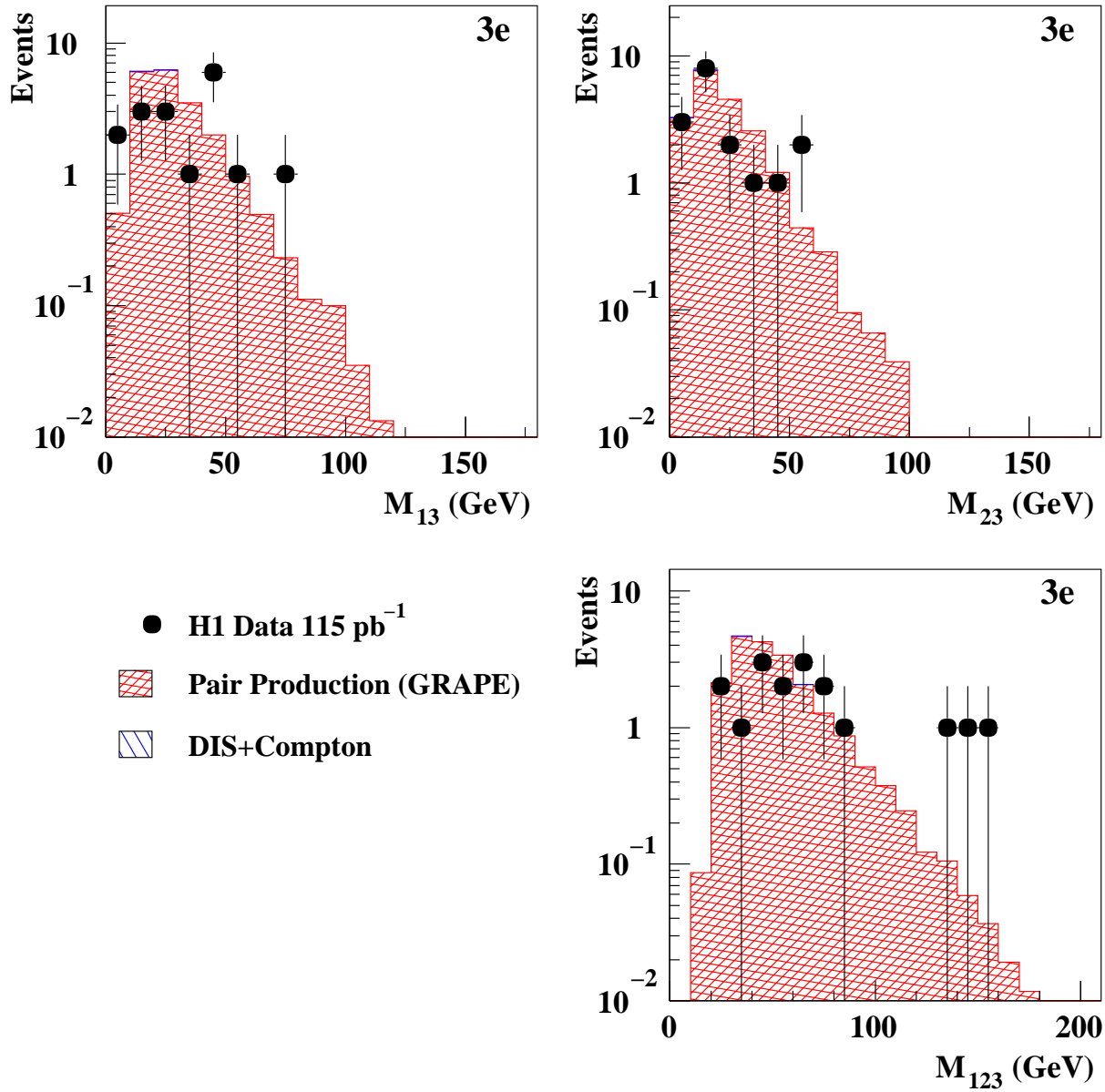


Figure 6: Invariant mass distributions of electron pairs 1-3 and 2-3 (top left and right) and of the tri-electron system (bottom right) for events classified as “3e”.

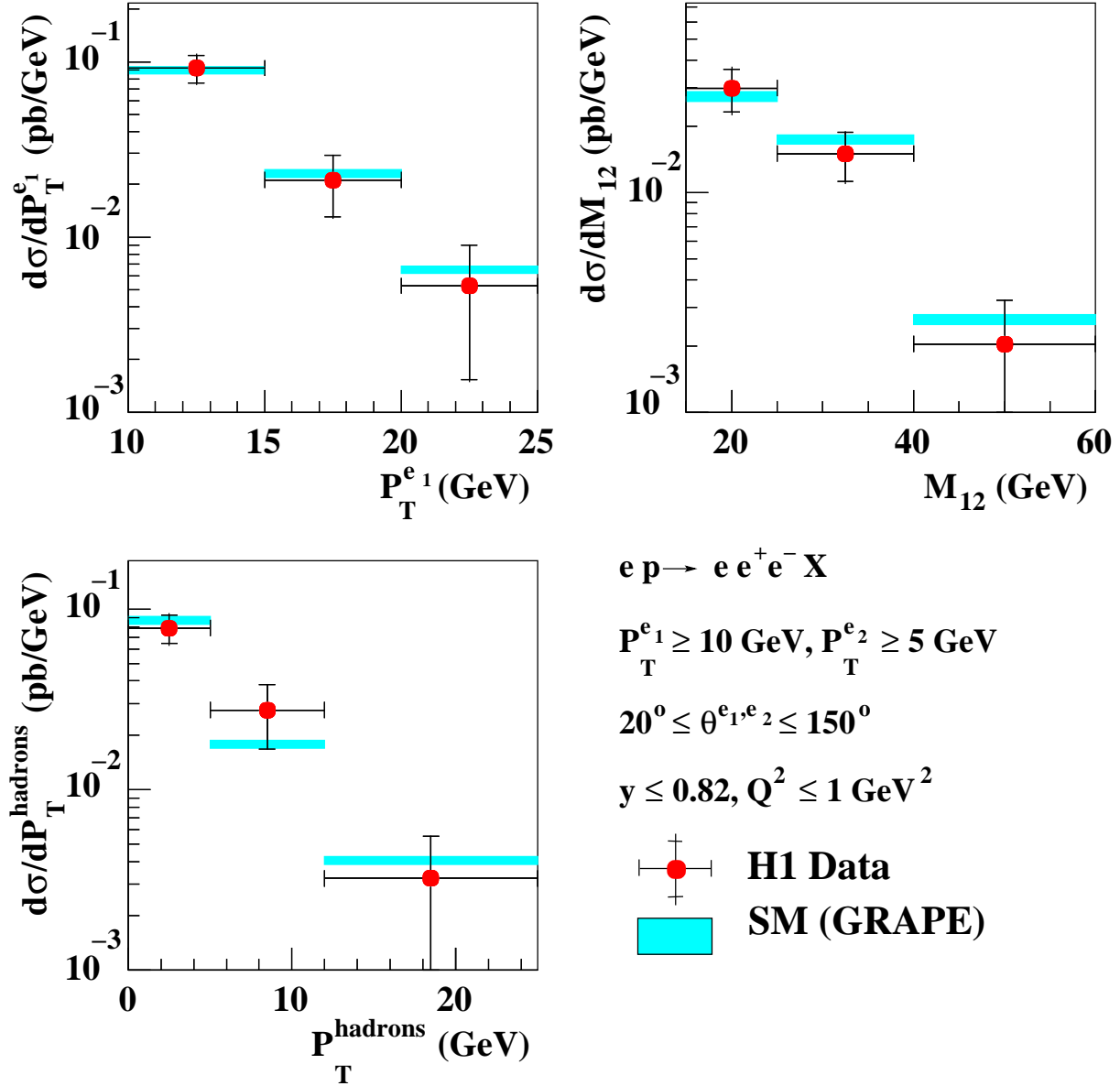


Figure 7: Cross section measurements in a restricted phase space dominated by the photon–photon process as a function of the leading electron transverse momentum (P_T^{e1}), the invariant mass of the electron–positron pair (M_{12}) and the hadronic transverse momentum (P_T^{hadrons}). The differential cross sections are averaged over the intervals shown. The inner error bars on the data points represent the statistical error, which dominates the measurement uncertainty. The outer error bars show the statistical and systematic uncertainties added in quadrature. The bands represent the one standard deviation uncertainty in the SM prediction.

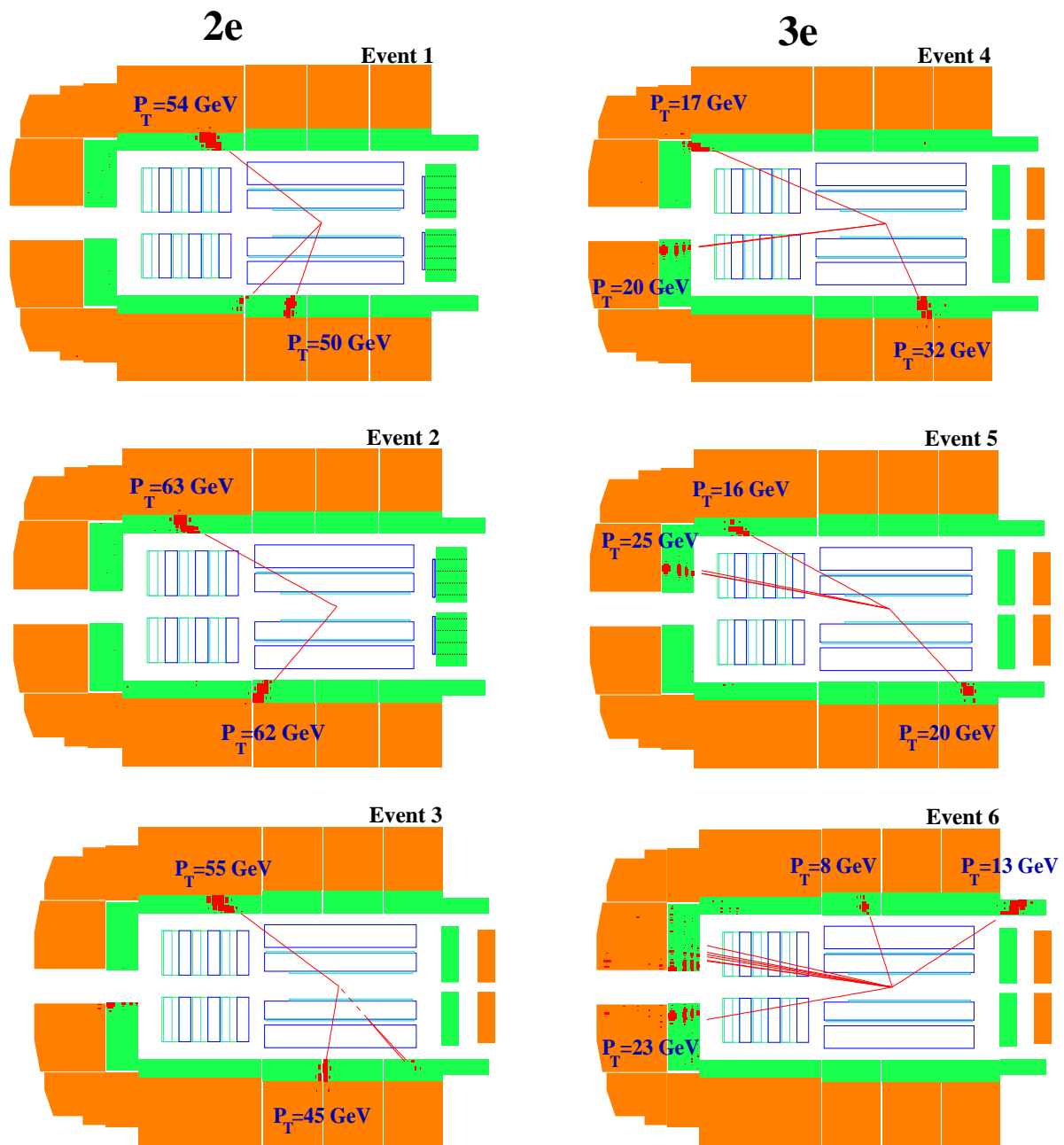


Figure 8: Displays of the three “2e” events (left) and the three “3e” events (right) with $M_{12} > 100$ GeV in the $R - z$ view. The reconstructed tracks and the energy deposits in the calorimeters are indicated (see text and table 4). The beam positrons enter the detector from the left and the protons from the right.